Chapter 3

Two dimensional heterostructure for efficient quantum energy storage as in-plane micro-supercapacitor

Portable miniaturized energy storage micro-supercapacitor has engrossed significant attention due to its power source and energy storage capacity, replacing batteries in ultra-small electronic devices. Fabrication with porous and 2D graphitic nanomaterials with high conductivity and surface area signify high performance of micro-supercapacitor. In order to satisfy the fast-growing energy demands for the next-generation, we present in this chapter the designing and performance of a 2D heterostructure of EDLC (g-C_3N_4) & pseudocapacitive ($FeNi_3$) resulting low ionic diffusion path and prominent charge storage based on their synergic functionalities. Moreover, the chapter is divided into two parts: Part A and Part B. Part A consist of experimental and Part B theoretical analysis.

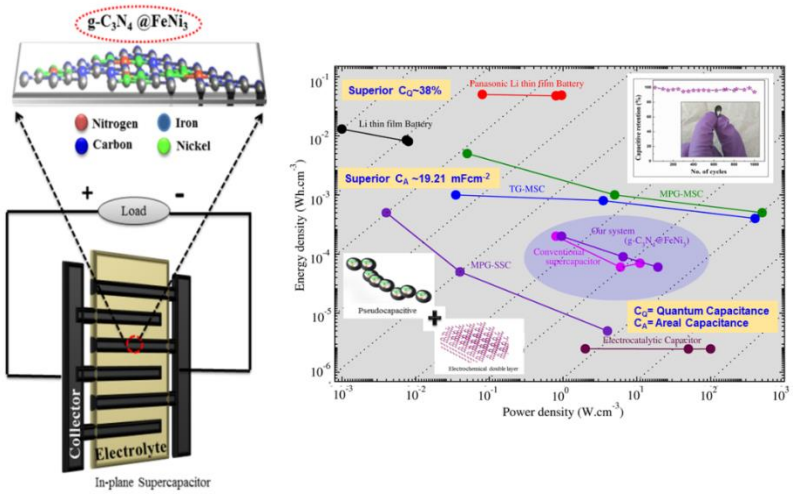

Figure 3.1: Schematic description of an in-plane micro-supercapacitor of g-C_3N_4@$FeNi_3$ heterostructure. Pseudocapacitive ($FeNi_3$) and electrochemical double layer (g-C_3N_4) are combined to form the heterostructure system.

This portion of the thesis is published in M. Talukdar et al. *Dalton Trans.*, **48**, (2019), 12137

3.1 Introduction

Rate of electric energy consumption has dramatically increased due to growing global population and fast development of modern industries. There is an unmet need of high-performance energy storing systems, where large amount of energy needs to be delivered or accepted within short period of time [1]. Micro-supercapacitors are promising energy storage device for future due to their high energy storage within small solid structure [2]. Compared to other batteries, in-plane designed micro-supercapacitors are preferred for developing electronic devices due to its unique properties in excellent rate capability, flexibility [3], stability and durable cycle life [4,5]. As battery performance has some limitations, in-plane micro-capacitors are the potential candidates to store the energy in miniaturized portable form directly on a chip meeting the demands and ensuring the adequate for future in-plane devices [6,7]. Electrochemical capacitors (EC) are attracting much attention towards storage of energy by redox reaction or by ion adsorption. EC acts as mediator between the energy and power electrostatic capacitors which works mainly on electrochemical double layer (EDL) and pseudo-capacitive materials. EDL follows ion adsorption, delivering higher power while pseudo-capacitive delivers higher energy density [8] suffering from redox reaction at the surface of the electrode. Future generation demands portable energy power source where supercapacitors with thinner, small sized and highly flexibility [9] as similar to micro-batteries will be required. In this case, designed and smart nanomaterials need to be developed which will act as storage source in the form of in-plane micro-supercapacitors overcoming the natural limits such as poor conductivity [10], instability and maximizing their significant advantages.

In this aspect, two dimensional (2D) materials with large surface area and abundance of reaction sites, shows high possibility of large charge storage capacitance [11] and better performances in terms of stability and flexibility. 2D materials also exhibit unique properties such as high power density, excellent rate performance and long cycle life [12], pushing the energy storage to the next level of stored specific charges. Owing to strong charge carrier localization, the

ionic conductivity [13] in two dimensional layered materials is efficient throughout the surface rather than between the layers [14]. Pseudocapacitive system with 2D material in composite will exhibit larger specific capacitances, whereas double layer type system exhibit better rate handling capability [15] and superior cycle longevity. In recent times, heterostructures have triggered great scientific and technological interests due to their high versatility as the essential components in quantum devices. Moreover, 2D heterostructures with efficient manipulation of physical property opens application possibilities in broad range of nano-electronic devices. Apart from its high surface area, the presence of mesopores within the sheet [16] helps in sufficient transportation of electrolyte shortening the diffusion distance. However, pseudocapacitive systems with fast reversible surface redox properties are required to improve the energy storage of EDLC materials. Iron based materials are promising materials for electrochemical devices because of their low cost, nontoxicity [17,18], good chemical stability and high energy-power density [19]. However, the materials suffer from aggregation after reaction, poor capacity retention and low electronic conductivity which hinder the electrolyte ions accessibility. Loading of nanoparticles on graphitic sheets can not only overcome these problems [20], but also minimize the aggregation or restacking of the nanosheets. Presence of high content of nitrogen in the 2D graphitic sheet can stabilize pseudocapacitive $FeNi_3$ redox material by escalating the metal-carbon binding energy and increases the capacitive performances. In this chapter, we have demonstrated the development of novel electrode using 2D mesoporous heterostructure material as an in-plane micro-supercapacitor for energy storage (shown in **Figure 3.1**). The electrode material is based on mesoporous carbon nitride embedded with redox $FeNi_3$ nanoparticles showing high areal capacitance performance. Presence of nitride content and mesopores in the two dimensional sheets provide more reaction sites for metal electrode allowing the electrolyte to efficiently exploit the surface. Also, synergic combination of both 2D carbon nitride and $FeNi_3$ nanoparticles will not only improve the physical properties, but also influences the rate of intercalation within the system due to continuous conducting pathway in carbon nitride. In

the present work, 2D g-C_3N_4 hybridizes with pseudocapacitive material for enhancement in electrochemical performances.

Part A

3.2 Methods

3.2.1 Development of 2D g-C_3N_4@$FeNi_3$ heterostructure: It is worth mentioning that development of the aforementioned system is discussed in the previous system i.e. in Chapter 2.

3.2.2 Materials Characterization: The working electrodes were prepared by mixing 80 wt% g-C_3N_4@$FeNi_3$ heterostructure, 15 wt% activated charcoal and 5 wt% Polyvinylidene fluoride (PVdF) with 1 ml N-Methyl-2-pyrrolidone (NMP), to form slurry. The slurry was pressed into a stainless steel grid of area (1 cm^2 × 1cm^2) and later dried in an oven at 70^0C for 10 hours. The electrochemical measurements were carried out in a three-electrode system with 1 M KOH and 2 M KOH as the aqueous electrolyte.

3.3 Results and Discussion

3.3.1 Microstructural and Surface Morphology Analysis

Microstructure and morphology of the prepared 2D heterostructure nanomaterial for in-plane supercapacitor shown in **Figure 3.2** was characterized by TEM and FESEM analysis. **Figure 3.2 (a, b)** shows the individual TEM images of graphitic carbon nitride and g-C_3N_4@$FeNi_3$ heterostructure material. **Figure 3.2 (a)** confirms the formation of mesopores in the sheets of carbon nitride. Advantage of mesopores in case of storage application is to create more channels for electrolyte ions to transport electrochemically [21], accessing more electroactive sites for energy storage faster. Also, porous materials act as the storage of ions and electrons resulting in improving the mass and charge transfer throughout the surface. **Figure 3.2 (b)** signifies the dispersion of homogeneous $FeNi_3$ nanoparticles with typical diameters 100-200 nm on the graphitic sheets with less aggregation. The uniformity and less aggregation will enable enhancement of the

electrochemical property. FESEM images showed in **Figure 3.2 (c)** reveals the formation of stacked graphitic sheets with spherical shaped $FeNi_3$ nanoparticles over the sheets.

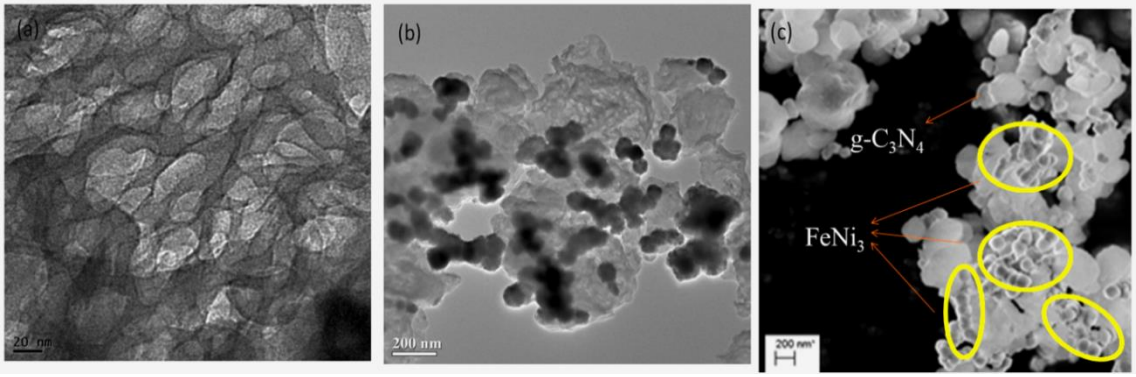

Figure 3.2: Microstructural characterization 2D heterostructure for in-plane micro-supercapacitor; **(a)**TEM micrograph of g-C_3N_4 and **(b)** g-C_3N_4@$FeNi_3$ heterostructure. **(c)** FESEM image of g-C_3N_4@$FeNi_3$.

AFM images of the system are shown (**Figure 3.3 a, b**) respectively for evaluating surface topology and roughness. The images reveal the thickness of the prepared multilayer g-C_3N_4@$FeNi_3$ heterosystem to be 50 nm. Justifying with the AFM results, **Figure 3.3 (b)** further signifies the formation of multilayer heterostructure system, where $FeNi_3$ is localised on the surface of g-C_3N_4 layers.

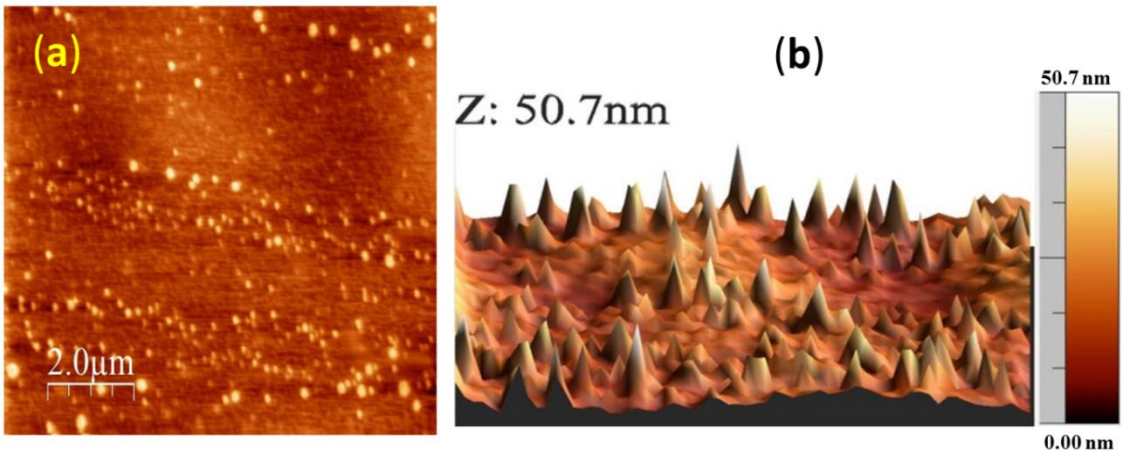

Figure 3.3: (a) Phase profile and **(b)** surface topology AFM images of g-C_3N_4@$FeNi_3$.

Raman analysis of g-C_3N_4@$FeNi_3$ (**Figure 3.4**) displays two peaks at 804 and 1782 cm^{-1}, assigned as D band and G band of graphitic carbon materials respectively. D band peak at 804 cm^{-1} corresponds to disordered carbon, which can be attributed to the defects and partially disordered structure of graphitic layers in the heterosystem. The broad bands at around 2429 cm^{-1} are characteristic of 2D graphitic carbon. Also, decrease in intensity ratio of I_D/I_G (ratio of 0.76) indicates no defects in the heterostructure system.

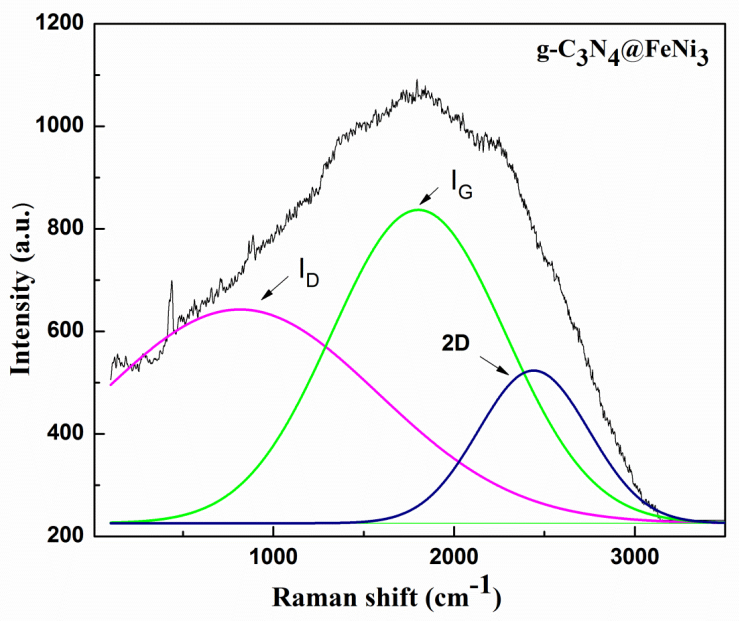

Figure 3.4: Raman curve for hybrid g-C_3N_4@$FeNi_3$ heterostructure

3.4 Electrochemical properties

Cyclic voltammetry studies and galvanostatic charge-discharge studies have been carried out in a three electrode system taking Ag/AgCl and Pt as the reference and counter electrode. The used electrolyte is KOH with two different concentrations (1M and 2M).

3.4.1 Cyclic voltammetry

Figure 3.5 reveals the cyclic voltammetry curves of the prepared g-C_3N_4@$FeNi_3$ heterosystem under various scan rates (25-200 mVs^{-1}). The curves remained unchanged, stable and nearly rectangular in shape indicating high flexibility and good electrochemical stability. Also, the quasi rectangular profile exhibiting

symmetry in shape, suggests an ideal capacitive behaviour of prepared heterostructure nanomaterial electrode. Such quasi-rectangular shape indicates that the mechanism of charge storage is due to electric double layer capacitance (EDLC) and Faradic reactions (pseudo capacitance) within the voltage range (-0.2V to + 0.6V). Moreover, redox peaks are completely absent during the CV scan which is due to the formation of double layer at the electrode and electrolyte interfaces. Because of the presence of OH^- ions in the electrolyte, there is a slight deviation in the curves indicating the reversible reaction.

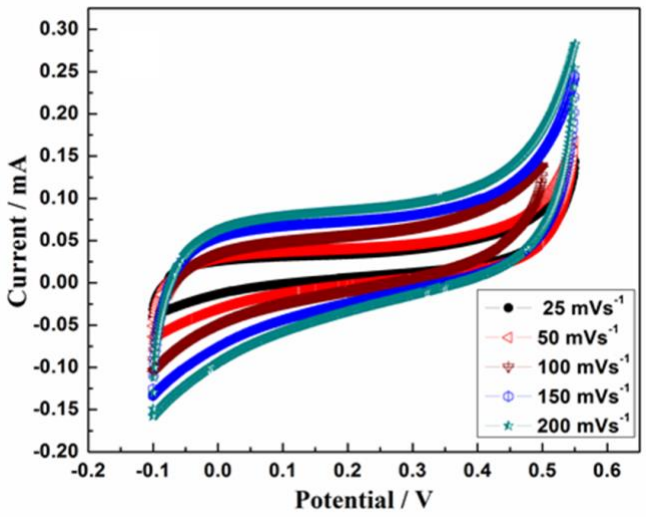

Figure 3.5: Electrochemical performance of g-C_3N_4@$FeNi_3$ heterostructure samples under three-electrode mode at different scan rates.

3.4.2 Galvanostatic charge discharge (GCD)

Figure 3.6 (a and b) shows the galvanostatic charge discharge (GCD) curve under various current densities with varying molar electrolyte concentration (KOH) at 1M and 2M. The discharge areal capacitance has been calculated using the formula,

$$C_a = \frac{I*t}{S*\Delta V}$$

where I is the applied current (mA), t is the time of discharge (s), S is the area of working electrode (cm^{-2}), and ΔV is the potential window. During GCD curve,

there is a voltage plateau observed in the first curve of 1M KOH electrolyte solution. The plateau is observed as a consequence of ion intercalation. This process creates interlayer spacing and expansion within the sheets leading to swelling of the electrode. Besides, it has been observed that increment in current density value results in reducing the plateau. Also, no straight voltage curve and height changing curves are seen in the GCD curve. It implies that the mechanism behind charge storage [22] is a mixture of both intercalation and adsorption. The areal capacitances are 5.12 $mFcm^{-2}$, 4.71 $mFcm^{-2}$ and 4.28 $mFcm^{-2}$ for 0.05 mA cm^{-2}, 0.15 mA cm^{-2} and 0.24 mA cm^{-2} current densities respectively, for electrolyte concentration of 1M KOH. Ion intercalation depends on the electrolyte concentration [23]. The ion intercalation decreases as we increase the electrolyte concentration to 2M KOH. On increasing the concentration of electrolyte, there is a formation of anion film above the surface of the sheets due to which no voltage plateau is observed in **Figure 3.6 (b)**. As a result, there is an increase in the areal capacitance of 19.21 $mFcm^{-2}$, 17.32 $mFcm^{-2}$ and 8.18 $mFcm^{-2}$ for 0.05 mA cm^{-2}, 0.15 mA cm^{-2} and 0.24 mA cm^{-2} current densities respectively, leading towards change in kinetics of the system. The reason behind the absence of plateau is due to the change or aggregation of dominant structure in the electrolyte which results in decrease in the potential of the superior electrolyte concentration [24]. Symmetry and linear curves at high current density indicates the excellent reversibility [25] during charge-discharge process. Limited migration of ions in electrode creates difficulty in charging process exhibiting decrease in specific capacitance on further increased in current density. Higher concentration of electrolyte promotes decreasing oxidation and reduction charges. At higher concentration of electrolyte, it was easier for the ions to transport within the electrode layers, leading to an effective building-up for double layer and hence increases the specific capacitance. However, if the concentration of electrolyte was low (i.e. 1M KOH), the diffusion current inside the pores get decreased, hence providing an insufficient number of ions for double-layer to build-up [26, 27].

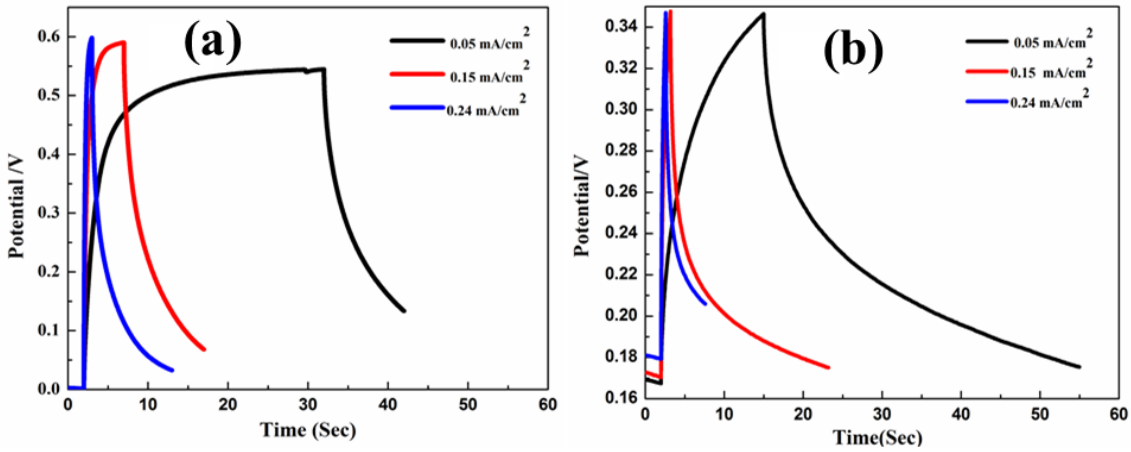

Figure 3.6: Galvanostatic charge discharge curve of the prepared heterostructure system at different current densities with **(a)** 1M KOH and **(b)** 2M KOH electrolyte concentration.

3.4.3 Impedance Spectroscopy

The Nyquist plot exhibits a larger slope and a shorter line suggesting a faster diffusion rate and smaller variation of the diffusion path. Nyquist plot as shown in **Figure 3.7 (a and b)** of the as prepared heterostructure material has been carried out under the frequency range of 0.30 MHz to 20 Hz, inset to the figure (**Figure 3.7 b**) showing the expanded high-frequency region of the same plot. In the curve, two distinct parts i.e. a small semicircle arc at high frequency region and a linear part at low frequency region can be seen. The vertical line at low-frequency region indicates the good capacitive behaviour and low diffusion resistance of the heterostructure nanomaterial. Nyquist curve of the g-C_3N_4@$FeNi_3$ heterostructure electrode exhibits very small arc and straight line, indicating ideal capacitive behaviour of the device and low resistance of the electrodes. At low frequency region, the presence of vertical line is due to the pseudocapacitive behavior of the electrode. Due to the presence of pseudocapacitive $FeNi_3$ NPs on g-C_3N_4, it offers resistance to the diffusion of the electrolyte ions within the pores of the g-C_3N_4, which improves the charge transfer performance of heterostructure electrode. This mechanism occurs due to the increase in electronic resistance, which is attributed to the broad band gap and poor conductivity of $FeNi_3$ NPs. Further the straight line in the low

frequency region, where diffusion of ions occurs due to sufficient wetting of the internal surface of porous electrode by the electrolyte, termed as Warburg resistance, represented the ion diffusion behavior in the electrode. As $FeNi_3$ are uniformly localized over the graphitic sheets, forming highly oriented inter-particle channels, the ion diffusion to the graphitic surface, especially for the deep segments of graphitic sheets near the substrate, is expedited. Hence, the combined effect of the charge transfer resistance reduction and the ion transport kinetics enhancement led to a substantial improvement of the electrochemical performance of the heterostructure for energy storage. The semi-circular loop at high frequency is too small to identify, indicating the small interfacial charge transfer resistance and good electrical conductivity of the electrode material which enables improved electronic and ionic conduction of the g-C_3N_4@$FeNi_3$ heterostructure. Here, the semicircle is ascribed to the charge transfer processes between the electrode and the electrolyte. It is clear that the system has smaller radius of semicircle indicating the smaller charge transfer impedance, which caused mainly due to two reasons. Firstly, presence of high molecular amount of nitrogen within the porous structures with high surface area enables rapid electrolyte diffusions and charge transfers providing good electronic conductivity. Secondly, the embedded $FeNi_3$ within the system may have reduced the charge transfer resistance of the pristine g-C_3N_4 leading to improved electronic and ionic conduction of the heterostructure electrodes through charge transfer interactions [28]. The high frequency arc of the system corresponds to the charge transfer limiting process and is ascribed to the double-layer capacitance due to the increased amount of nitrogen content and higher carbonization degree, which ultimately improves the conductivity in contact with the interface between the electrode and electrolyte solution. From the morphology of the system, it is clear that a large amount of $FeNi_3$ nanoparticles exists on the high surface area of g-C_3N_4, which increases the polarity of the layered material. The presence of high content of nitrogen creates ability for the accumulation of charges, which is beneficial to the charge transfer. This ultimately improves the conductivity due to higher carbonization degree. Further, the unique porous

structure and the intimate interaction between g-C_3N_4@$FeNi_3$ are also beneficial for the charge transfer. The π-π stacking interaction between the heterostructure system and the electrolyte further enhances the electron-transfer efficiency for the composite material, which reduces the internal resistance.

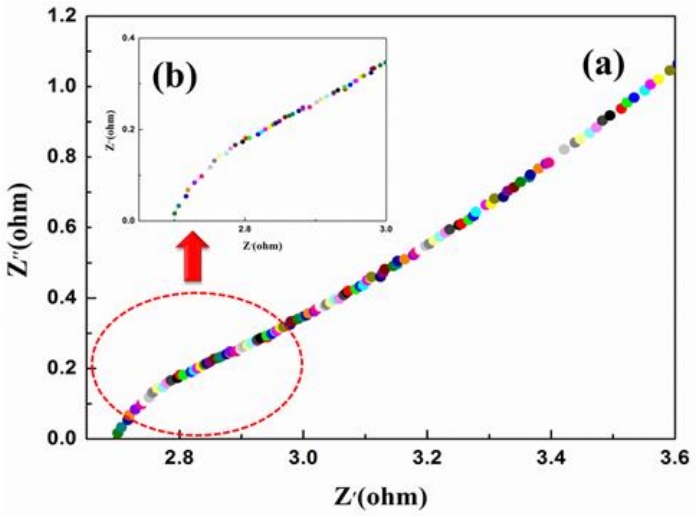

Figure 3.7: (a) Nyquist plot of the electrode. **(b)** inset shows the enlarged high-frequency region.

3.4.4 Cyclic performances

Figure 3.8 (a) shows the comparison result of areal capacitances of the heterosystem in 3D visual. Also, the cyclic performance has been tested up to 1000 cycles, at 150 mVs^{-1} scan rate as shown in **Figure 3.8 (b)**. The shape of the curves at various cycles showed in **Figure 3.8 (c)** inset remains unchanged. The capacitive retention obtained is 94% after 1000^{th} cycle indicating extremely stable behaviour of the system. In this heterostructure system, $FeNi_3$ nanoparticles are present uniformly on the surface of the graphitic sheets. Subsequently, a binder (polyvinylidene difluoride, PVDF) is used to cover the heterostructure system in order to obtain slurry condition which is suitable for performing good electrochemical properties. Further, large number of visible pores within the system can effectively decrease the ion transport dimensions for further shortening of ion diffusion length. During cycling process, agglomeration as well as pulverization effects of the $FeNi_3$ nanoparticles are controlled by the PVDF

binder maintaining an optimized ratio. Thus, as-prepared heterostructure of porous graphitic C_3N_4 material along with $FeNi_3$ nanoparticles with PVDF binder provides strong adhesion between the electrode film and the current collector as well as uniform particle distribution of conducting networks. This provides shorter diffusion length and good electrolyte percolation which helps for easy release of the generated strain during cycling process retaining the morphology of the system after the cycles [29]. Thus, it is obvious that the surface morphology of the system is retained after 1000 cycles. Further the developed material attains high stability and capacitive retentivity showing a promising candidate in electronic device application.

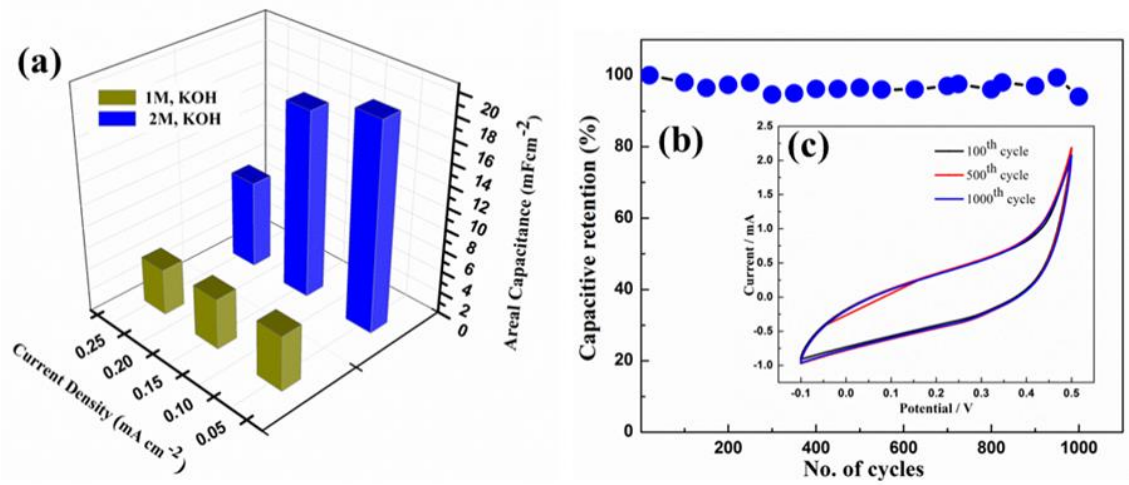

Figure 3.8: (a) Comparative study 3D visualization graph for areal capacitance of the heterostructure. **(b)** Cycling capacity of the g-C_3N_4@$FeNi_3$ heterostructure. **(c)** inset shows the stability of the system after its 1000^{th} cycle.

3.5 Device Strategy

In order to explain the design of the in-planar micro-supercapacitor, **Figure 3.9** depicts a schematic illustration showing the mechanism of the charge-discharge phenomenon of the developed heterostructure system. The in-plane device is architecture with both electro-chemical double layer and pseudo capacitive material where the ions move horizontally within the sheets resulting low ionic diffusion path and prominent charge storage. The material can be folded to 360 degree which suits the requirement of flexibility and ability stretch. In these

aspects, 2D graphitic C_3N_4 material with high surface area and porous nature provide full access to the electrolyte ions in storage capacity. The hexagonal channels in g-C_3N_4 are providing potential binding sites for the intercalated cations. Such planar geometry of the 2D g-C_3N_4@$FeNi_3$ heterostructure is enabling the design of the device with high areal capacitance, flexibility and stability. Apart from its convenient architecture, the extensive duration in discharge time and the high areal specific capacitance of the 2D heterostructure promise for high-performance in-plane micro-supercapacitor for future generation. The extensive duration in discharge time occurs mainly due to two reasons (i) due to conductivity enhancement in ion transport in count with charge storage by 2D sheets and also reduction of the mobile resistance of the ions by redox nanoparticles by preventing aggregation of the 2D sheets (ii) due to the mesoporous architecture in carbon nitride which reduces the ion transport resistance and ion diffusion distance, enhancing the charge storage.

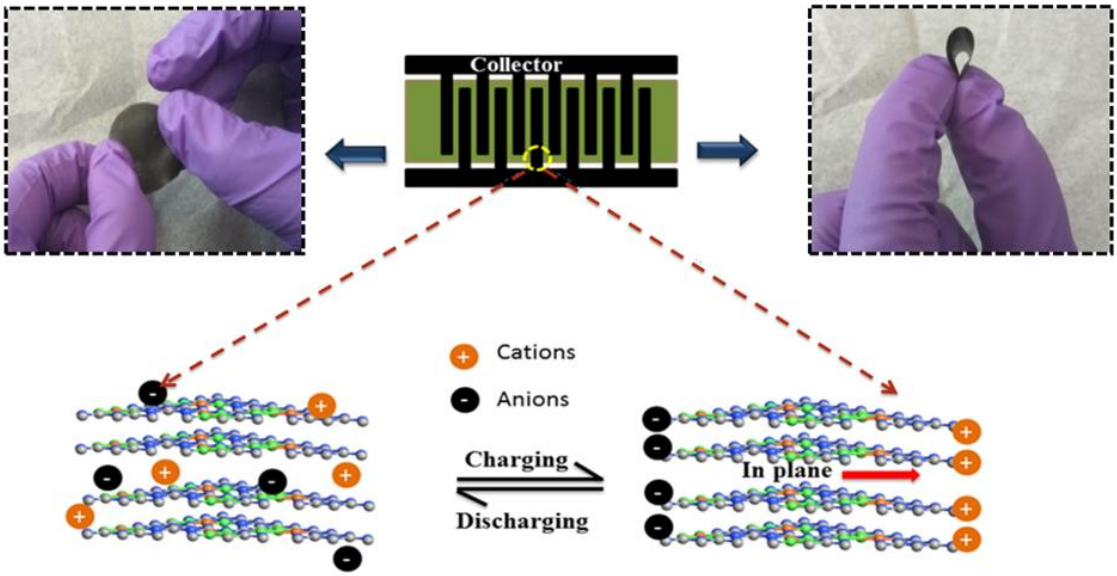

Figure 3.9: Mechanism for the device fabrication using 2D g-C_3N_4@$FeNi_3$ heterostructure.

PART B

3.6 Theoretical Analysis

3.6.1 Density functional theory calculation: Here *ab initio* calculations were performed within the framework of density functional theory (DFT) using a local density approximation scheme, as implemented in QUANTUM Espresso code. The generalized gradient approximation (GGA) for the exchange correlation functional with the parametrization of Perdew-Burke-Ernzerhof (PBE) was used during the computational calculation. The core electrons were represented by Projector augmented wave (PAW) pseudopotentials via real space integration on a plane-wave grid expansion at a kinetic energy cutoff of 780 eV. In all cases, the systems have been relaxed via Broyden method until the forces on all atoms were less than 0.005 eV/Å. During the periodic DFT calculation, we followed a 16×16×1 Monkhorst-Pack *k*-point sampling for Brillouin-Zone integration in geometry optimization and 27×27×1 k-point mess for electronic structure calculation. We considered a hexagonal supercell for designing the geometric structure of g-C_3N_4. The supercell contains 3×3×1 units with 112 atoms in order to simulate possible stacking configurations of the sheet structure. A vacuum gap of 12 Å in the z-direction was maintained throughout this computation to avoid interactions of the graphitic sheet with its periodic images. The Green's function and the screened Coulomb interaction due to presence of metal atoms were considered within DFT simulation. The Gibbs surface free energy profiles were obtained from the 3×3×1 supercell. The total energy from DFT calculations were obtained as $E^{tot} = [E(Composite) - E(Pristine) - \frac{n}{2}E(G)]$, Thermal corrections were implemented to calculate adsorption free energy profile. Zero-point energy and temperature dependent entropy contribution are included to find final free energy. The Gibbs free energy of the system was calculated as $E(G) = E_{tot} + 0.22$ eV.

3.6.2 Quantum Capacitance Calculation: It is obvious that an ideal metal with perfect screening will cause the confinement of excess charge on the surface of

the metal atom embedded heterostructure system. Therefore, the capacitance of metal contact as a part of the electrode hardly plays any role and can be skipped during the calculation. [30] Carbon based materials are not with good screening when they are used as the electrode materials. Thus, it will be possible for the intrinsic capacitance (called as quantum capacitance, C_Q) to have a significant effect on device performance, such as supercapacitor. The quantum capacitance is defined as, $C_{Q=} {}^{d\sigma}/_{d\emptyset_G}$, where dσ and $d\Phi_G$ are the differential of charge density and local potential. If it is assumed that the electrochemical potential can be shifted rigidly by $e\emptyset_G$, the excess charge density can be expressed as, $\Delta Q = \int_{-\infty}^{\infty} D(E)[f(E) - f(E - e\Phi_G)]dE$, where, D(E) and *f*(E) are the DOS and Fermi-Dirac distribution function, respectively. E is the relative energy with respect to Fermi level E_F. For pristine graphene, if the temperature effect is ignored, the quantum capacitance can be expressed as, $C_Q = e^2 \frac{g_s g_v}{2\pi(\hbar V_F)^2}|e\Phi_G|$, where g_s(=2) and g_v(=2) are the spin and valley degeneracies of graphene, $\hbar$ is the Planck constant, and V_F (~10^8 cm.s^{-1}) is the Fermi velocity of carriers near the Dirac point. For other graphene based 2D materials, by the analytical expression of ΔQ, the quantum capacitance has been written as, $C_Q = e^2 \int_{-\infty}^{\infty} D(E)F_T(E - e\Phi_G)dE$, where F_T(E) is the thermal broadening function and expressed as, $F_T(E) = (4k_BT)^{-1}\,\mathrm{sech}^2({}^{E}/_{2k_BT})$, where k_B is Boltzmann's constant. Room temperature (i.e. 300 K) is considered to be the temperature parameter (T) in the calculation of quantum capacitance. Moreover, *D(E)* derived from DFT calculation is restructured with high precision by the linear interpolation method during the whole computational work for the integral calculation.

3.7 Results and Discussions

3.7.1 Geometrical optimization

The minimum energy sustained geometry of the heterostructure system along with pristine form of graphitic sheets is fixed via optimization of surface atomic configuration. The optimization is followed by moving the atoms assisted with the structure to the minimum energy positions for accurate stability during computation. The stable geometry of the systems is shown in **Figure 3.10 (a) to (c)**. The geometry and corresponding interlayer distances are determined by employing the atomic structure optimization with the van der Waals (vdW) corrections. It is observed that presence of metallic atoms (i.e. Fe and Ni) on the graphitic sheet surface make the heterostructure system stable at higher total surface energy compared to its pristine sheet. The stable atomic configuration of g-C_3N_4 (shown in **Figure 3.10 (a)**) sheet achieved the minimum energy stability at -768.83 Ry, whereas the monolayer heterostructure (g-C_3N_4@$FeNi_3$) (**Figure 3.11**) showed energy value of -1068.09 Ry. In supercell structure**,** the stable energy has achieved a value of -964.25 Ry. The enhancement in surface free energy value in heterostructure system controls the electronic structure and makes them dynamic towards the molecular motion with enhanced kinetic energy compared to pristine system.

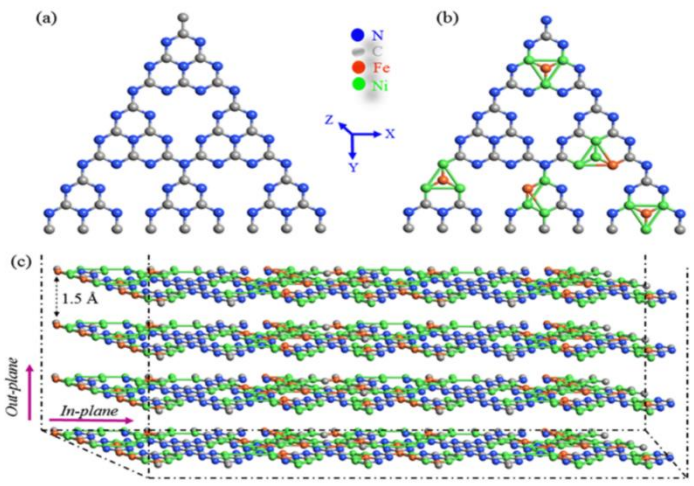

Figure 3.10: Optimized geometry. **(a)** g-C_3N_4 and **(b)** g-C_3N_4@$FeNi_3$ heterostructure from the top view. **(c)** Multi-layered heterostructure system with an interlayer spacing of 1.5 Å in a supercell of 3×3×1 units marked with black dotted line. Pink coloured arrows marks are shown to distinct out-plane and in-plane direction of the supercell model for easy understanding of the calculation method with respect to the Cartesian coordinate system.

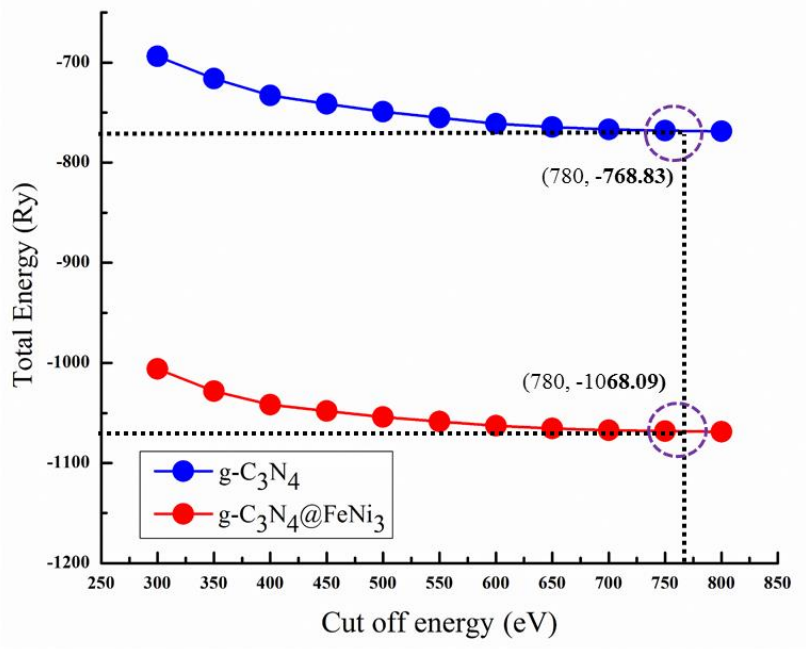

Figure 3.11: The total energy variation as a function of cut-off energy of the system gained after geometry optimization to achieve structural stability via BFGS algorithm.

3.7.2 Local densities of states (LDOS)

Local densities of states (LDOS) (**Figure 3.12 (a) and (b)**) have been calculated to understand the origin and control of molecular motion for energy storage activity of the active sites formed in g-C_3N_4@$FeNi_3$ heterostructure system. Overlapping states are observed from the plots of the density of states showing the dynamic and metallic behaviour in the monolayer and multilayer systems compared to their pristine sheet. Presence of localized electrons due to embedded metal atoms (Fe and Ni atoms) over g-C_3N_4 surface contributed towards the formation of overlapping states at Fermi level within conduction band and improved conductivities with delocalized nature of the active metal sites. Carbon and nitrogen atom orbitals show significant states, which are delocalized in heterostructure system unlike their localized nature in pristine g-C_3N_4 sheet. Moreover, this delocalized electronic behaviour supports in achieving highly negative surface Gibbs free energy value. This nature helps in maintaining the metallic behaviour of the heterostructure system for easy energy storage.

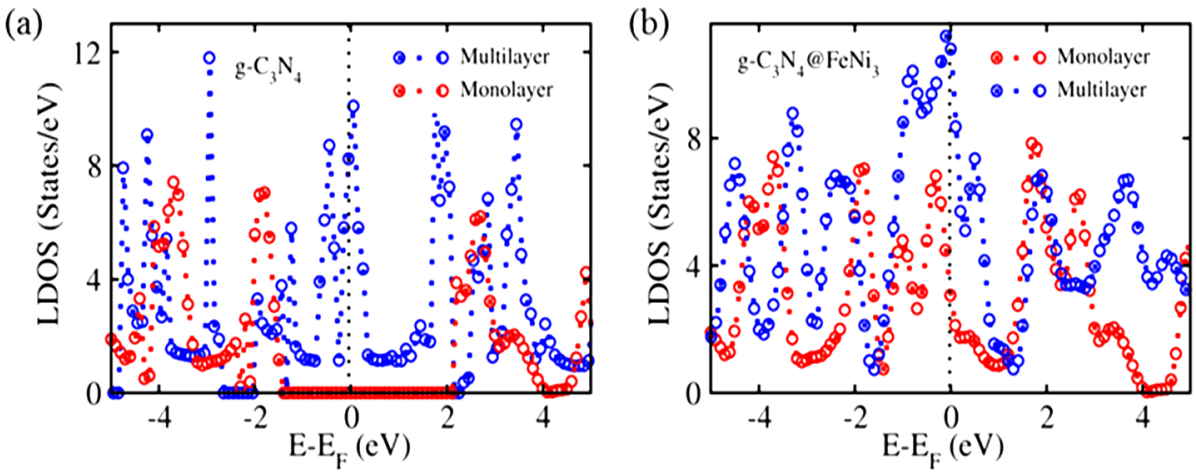

Figure 3.12: Local density of states (LDOS) calculation for both. **(a)** g-C_3N_4 and **(b)** g-C_3N_4@$FeNi_3$ heterostructure system. In both cases, monolayer and multi-layered sheets are considered.

3.7.3 Projected density of states (PDOS)

To realize the orbital existence and contribution, the DOS pattern has been projected in reciprocal *k*-space to get projected crystal wave function values named as projected density of states (PDOS). Here, we have resolved the case for both pristine and heterostructure system to show the PDOS (shown in **Figure 3.13 (a) and (b)**) pattern. The PDOS pattern clearly indicates the reflection of all orbitals of the constituent atoms (i.e. carbon, nitrogen, iron and nickel) in monolayer and multi-layer pattern of the systems. It is noticed that there is no enhancement in projection densities of the systems in both monolayer and multilayer case. This confirms equal contribution and overall projection of all atomic orbitals that are present in the pristine and heterostructure systems. This PDOS pattern reflects the orbital splitting which can be corroborated with respective electronic band structure in (**Figure 3.14 (a) to (d)**). We have noticed that in the presence of Fe and Ni atoms on g-C_3N_4 surface, the band gap is completely closing indicating an overlapping metallic stage. This can be attributed to the effect of metal atoms on graphitic sheet substrate to retain the metallic nature in the heterostructure system.

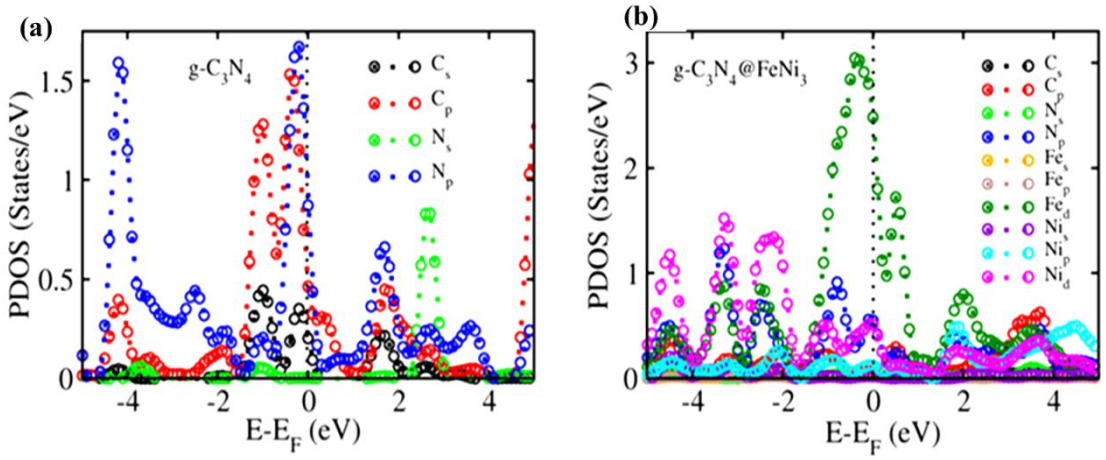

Figure 3.13: Partial density of states (PDOS) are shown for **(a)** g-C_3N_4 and (**b)** g-C_3N_4@$FeNi_3$ heterostructure system. Fermi energy level is shown with black dotted line.

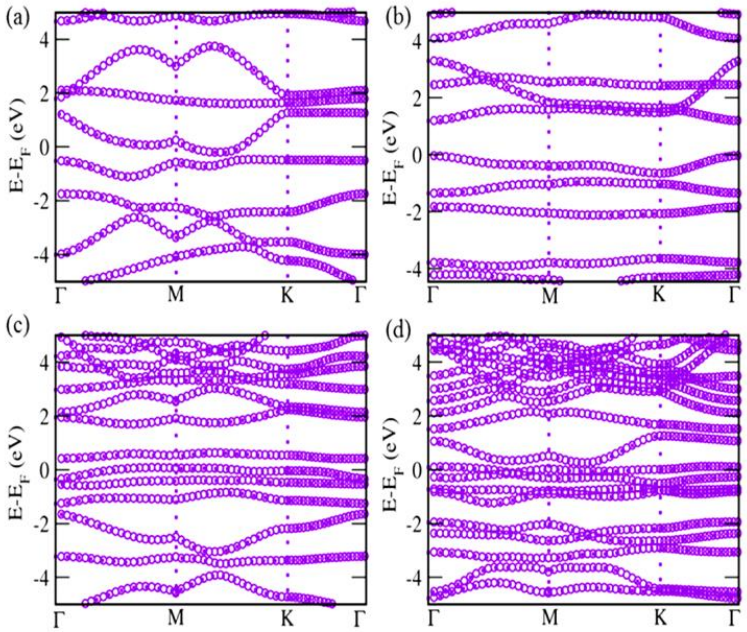

Figure 3.14: Electronic Band Structure of **(a)** g-C_3N_4 and **(b)**, g-C_3N_4@$FeNi_3$ heterostructure system are shown. Similarly, the band structure of respective multilayer systems is shown in **(c)** g-C_3N_4 and **(d)** g-C_3N_4@$FeNi_3$ heterostructure. The bands are plotted along the symmetric k-points of Γ-M-K-Γ direction.

3.7.4 Quantum capacitance

The value of quantum capacitance is (C_Q) shown in (**Figure 3.15 a**). It is observed that C_Q=174.6 μF.cm^{-2} for heterostructure, whereas the pristine g-C_3N_4 gains 126.4 μF.cm^{-2} value at electrode potential of 0 V. This intense improvement (almost 38%) in C_Q value is apparently because of the readily available enhanced density states near the Fermi level with a contribution from the additional metallic (Fe and Ni) states and shifting of the Dirac point (corroborated with **Figure 3.12 and 3.13**). To demonstrate the overall performance of this 2D heterostructure in-plane supercapacitor, a Ragone plot is shown in **Figure 3.15 b**. The data from Max Plank Group (MPG) based sandwich-supercapacitor (MPG-SSC) and T-Graphene based micro-supercapacitor (TG-MSC), as well as a commercial high-energy lithium thin-film battery,[31] high-power aluminium electrolytic capacitor [32] and Panasonic Li-ion battery [33] are included for comparison and standing of the present system as a supercapacitor. MPG-MSCs [34] reported a volumetric

energy density of 0.0038 Wh.cm^{-3}, which is an order of magnitude higher than that of the typical supercapacitor of activated carbon (<1 Wh cm^{-3}), and well comparable to that of lithium thin-film batteries (10^{-3}-10^{-2} Wh.cm^{-3}). In addition, MPG-MSCs manifest an ultrahigh power density of 512 W.cm^{-3} (even at a high energy density of 0.018 Wh cm^{-3}) discharging within an extremely short time (~1ms). The power density of the present system is approximately 17 times higher than that of conventional supercapacitor having energy density value of 0.30 Wh.cm^{-3}. To the best of our knowledge, this is the first report of heterostructure in-plane micro-supercapacitor having excellent performance in terms of high power and energy densities. Therefore, this miniaturized in-plane micro-supercapacitor can provide a nano or micro-scale power source to meet the applications that require higher operating currents and voltages in a short time-frame.

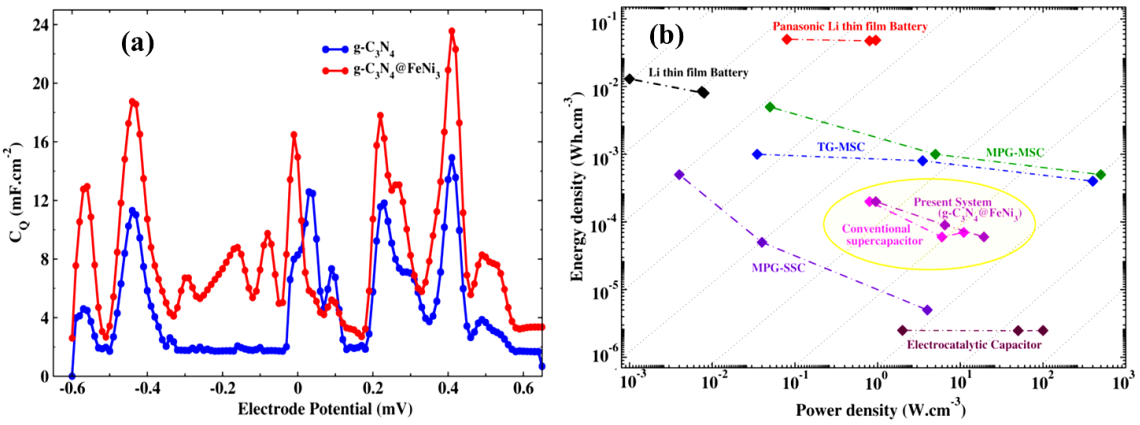

Figure 3.15: (a) Calculated quantum capacitance (C_Q) as a function of the electrode potential and **(b)** Ragone plot of the heterostructure g-C_3N_4@$FeNi_3$ system compared with other reported systems.

3.8 Conclusion

In this chapter we demonstrated an effective strategy for the development of an electrode using g-C_3N_4@$FeNi_3$ heterostructure. Graphitic carbon nitride with highly mesoporous nature effectively enhanced the transmission of ions and electrons. Simultaneously $FeNi_3$ nanoparticles prevented the aggregation of graphitic layers by increasing the areal capacity of the system. Complete

electronic structure and quantum capacitance of the heterostructure system have been investigated systematically. The DFT simulations show that the heterostructure generates new delocalized electronic states, consequently enhance overlapping states in band structure near Fermi level and derive 38% enhancement in quantum capacitance. The synergic effect of both electro double layer and pseudocapacitive components provide several electron channels for ion transfer within the system. The power density (with superior high energy density of 0.30 $Wh.cm^{-3}$) of this system is approximately 17 times higher than that of conventional available supercapacitor. Apart from high areal capacitance, capacitive retention, excellent stability and flexibility, the unique strategy of the present heterostructure system is the long duration in discharge time which occurred due to conductivity enhancement in ion transport, making the system a promising candidate for ultrahigh performance in-plane micro-supercapacitor for future generation.

References

[1]Agrawal, R., and Wang, C. On-Chip Asymmetric Microsupercapacitors Combining Reduced Graphene Oxide and Manganese Oxide for High Energy-Power Trade off. *Micromachine,* 9(8):399-413, 2018.

[2]Chen, J., Yang, B., Liu, L., Su, L., Shen, B., and Yan, X. In-Plane Micro-Supercapacitors for an Integrated Device on One Piece of Paper. *Advanced Functional Materials,* 27(43):1702394-1702405, 2017.

[3]Shen, L., Lv, H., Chen, S., Kopold, P., Aken, P. A. van., Wu, X., Maier, J., and Yu, Y. Peapod-like Li_3VO_4/N-Doped Carbon Nanowires with Pseudocapacitive Properties as Advanced Materials for High-Energy Lithium-Ion Capacitors. *Advanced Materials,* 29(27):1700142-1700150, 2017.

[4]Liang, K., Tang, X., Hu, W., and Yang, Y. Ultrafine V_2O_5 Nanowiresin 3D Current Collector for High-Performance Supercapacitor. *ChemElectroChem,* 3:704-708, 2016.

[5] Kennaz, H., Harat, A., Guellati, O., Momodu, D. Y., Barzegar, F., Dangbegnon, J. K., Manyala, N., and Guerioune, M. Synthesis and

electrochemical investigation of spinel cobalt ferrite magnetic nanoparticles for supercapacitor application. *Journal of Solid State Electrochemistry,* 22(3):835-847, 2018.

[6] Liu, L., Li, H. Y., Yu, Y., Liu, L., and Wu, Y. Silver nanowires as the current collector for a flexible in-plane micro-supercapacitor via a one step, mask-free patterning strategy. *Nanotechnology,* 29(5):055401-055411, 2018.

[7] Da, Y., Liu, J., Zhou, L., Zhu, X., Chen, X., and Fu, L. Engineering 2D Architectures toward High-Performance Micro-Supercapacitors. *Advanced Materials,* 33(1):1802793-1802821, 2018.

[8] Wu, Z. S., Parve, K., Feng, X., and Mullen, K. Graphene-based in-plane micro-supercapacitors with high power and energy densities. *Nature Communications,* 4:2487-2495, 2013.

[9] Huang, G. W., Li, N., Du, Y., Feng, Q. P., Xiao, H. M., Wu, X. H., and Fu, S. Y. Laser-Printed In-Plane Micro-Supercapacitors: From Symmetric to Asymmetric Structure. *ACS Applied Materials & Interfaces,* 10:723-732, 2018.

[10] Aytug, T., Rager, M. S., Higgins, W., Brown, F. G., Veith, G. M., Rouleau, C. M., Wang, H., Hood, Z. D., Mahurin, S. M., Mayes, R. T., Joshi, P. C., and Kuruganti, T. Vacuum-Assisted Low-Temperature Synthesis of Reduced Graphene Oxide Thin-Film Electrodes for High-Performance Transparent and Flexible All-Solid-State Supercapacitors. *ACS Applied Materials & Interfaces,* 10:11008-11017, 2018.

[11] Behera, S. K., and Deb, P. Controlling the bandgap in graphene/h-BN heterostructures to realize electron mobility for high performing FETs. *RSC Advances,* 7:31393-31400, 2017.

[12] Yu, S., Zhang, Y., Lou, G., Wu, Y., Zhu, X., Chen, H., Shen, Z., Fu, S., Bao, B., and Wu, L. Synthesis of NiMn-LDH Nanosheet@Ni_3S_2 Nanorod Hybrid Structures for Supercapacitor Electrode Materials with Ultrahigh Specific Capacitance. *Scientific Reports,* 8:5246-5258, 2018.

[13] Yao, C., Li, G., Wang, J., Xu, Y., and Chang, L. Template-free synthesis of porous carbon from triazine based polymers and their use in iodine adsorption and CO_2 capture. *Scientific Reports,* 8:1867-1876, 2018.

[14] Wang, S., Yu, Y., Li, R., Feng, G., Wu, Z., Compagnini, G., Gulino, A., Feng, Z., and Hu, A. High-performance stacked in-plane supercapacitors and supercapacitor array fabricated by femtosecond laser 3D direct writing on polyimide sheets. *Electrochimica Acta,* 241:153-161, 2017.

[15] Jayaramulu, K., Dubal, D. P., Nagar, B., Ranc, V., Tomanec, O., Petr, M., Datta, K. K. R., Zboril, R., Gómez-Romero, P., and Fischer, R. A. Ultrathin Hierarchical Porous Carbon Nanosheets for High-Performance Supercapacitors and Redox Electrolyte Energy Storage. *Advanced Materials,* 30(15):1705789-1705798, 2018.

[16] Li, B., Zheng, J., Zhang, H., Jin, L., Yang, D., Lv, H., Shen, C., Shellikeri, A., Zheng, Y., Gong, R., Zheng, J. P., and Zhang, C. Electrode Materials, Electrolytes, and Challenges in Nonaqueous Lithium-Ion Capacitors. *Advanced Materials,* 30(17):1705670-1705689, 2018.

[17] Whittingham, M. S. Lithium Batteries and Cathode Materials. *Chemical Reviews,* 104:4271-4301, 2004.

[18] He, Y., Zhang, P., Wang, M., Wang, F., Tan, D., Li, Y., Zhuang, X., Zhang, F., and Feng, X. Nano-sandwiched metal hexacyanoferrate/graphene hybrid thin films for in-plane asymmetric micro-supercapacitors with ultrahigh energy density. *Materials Horizons,* 6:1041-1049, 2019.

[19] Guo, R., Chen, J., Yang, B., Liu, L., Su, L., Shen, B., and Yan, X. In-Plane Micro-Supercapacitors for an Integrated Device on One Piece of Paper. *Advanced Functional Materials,* 27(43): 1702394-1702405, 2017.

[20] Fan, M., Wu, J., Yuan, J., Deng, L., Zhong, N., He, L., Cui, J., Wang, Z., Behera, S. K., Zhang, C., Lai, J., Jawdat, B. M. I., Vajtai, R., Deb, P., Huang, Y., Qian, J., Yang, J., Tour, J. M., Lou, J., Chu, C. W., Sun, D., and Ajayan, P. M. Doping Nanoscale Graphene Domains Improves Magnetism in Hexagonal Boron Nitride. *Advanced Materials,* 31(12):1805778-1805787, 2019.

[21] Tkatchenko, A., and Scheffler, M. Accurate molecular van der Waals interactions from ground-state electron density and free-atom reference data. *Physical Review Letters,* 102:073005-073009, 2009.

[22] El Kady, M. F., Strong, V., Dubin, S., and Kaner, R. B. Laser scribing of high-performance and flexible graphene-based electrochemical capacitors. *Science,* 335:1326-1330, 2012.

[23] Nagasubramanian, G., Jungst, R. G., and Doughty, D. H. Impedance, power, energy, and pulse performance characteristics of small commercial Li-ion cells. *Journal of Power Sources,* 83:193-203, 1999.

[24] Wu, Z. S., Parvez, K., Feng, X., and Müllen, K. Graphene-based in-plane micro-supercapacitors with high power and energy densities. *Nature Communication,* 4:2487-2495, 2013.

[25] Talukdar, M., Behera, S. K., Bhattacharya, K., and Deb, P. Surface modified mesoporous g-C_3N_4@$FeNi_3$ as prompt and proficient magnetic adsorbent for crude oil recovery. *Applied Surface Science,* 473:275-281, 2019.

[26] Giannozzi, P. et al., QUANTUM ESPRESSO: a modular and open-source software project for quantum simulations of materials. *Journal of Physics: Condensed Matter,* 21:395502-395522, 2009.

[27] Perdew, J. P., Burke, K., and Ernzerhof, M. Generalized Gradient Approximation Made Simple. *Physical Review Letters,* 77:3865-3869, 1996.

[28] Monkhorst, H. J., and Pack, J. D. Special points for Brillouin-zone integrations. *Physical Review B,* 13:5188-5192, 1976.

[29] Paek, E., Pak, A. J., and Hwang, G. S. A Computational Study of the Interfacial Structure and Capacitance of Graphene in [BMIM][PF6] Ionic Liquid. *Journal of The Electrochemical Society,* 160:A1-A10, 2013.

[30] Paek, E., Pak, A. J., Kweon, K.E., and Hwang, G. S. On the Origin of the Enhanced Supercapacitor Performance of Nitrogen-Doped Graphene. *The Journal of Physical Chemistry C,* 117:5610-5616, 2013.

[31] Pech, D., Brunet, M., Durou, H., Huang, P., Mochalin, V., Gogotsi, Y.,Taberna, P. L., and Simon, P. Ultrahigh-power micrometre-sized supercapacitors based on onion-like carbon. *Nature Nanotechnology*, 5:651–654, 2010.

[32] Kady, M. F. El., Strong, V., Dubin, S., and Kaner, R. B. Laser scribing of high-performance and flexible graphene-based electrochemical capacitors. *Science*, 335:1326–1330, 2012.

[33] Nagasubramanian, G., Jungst, R. G., and Doughty, D. H., Impedance, power, energy, and pulse performance characteristics of small commercial Li-ion cells. *Journal of Power Sources,* 83:193–203, 1999.

[34] Wu, Z. S., Parvez, K., Feng, X., and Müllen, K. Graphene-based in-plane micro-supercapacitors with high power and energy densities. *Nature Communication*, 4:2487-2495, 2013.